AIAA-2002-2411

Unsteady Simulation of a Landing-Gear Flow Field

F. Li
High Technology Corporation
Hampton, VA

M. R. Khorrami
NASA Langley Research Center
Hampton, VA

M. R. Malik
High Technology Corporation
Hampton, VA

8th AIAA/CEAS Aeroacoustics Conference
17–19 June 2002
Breckenridge, Colorado

UNSTEADY SIMULATION OF A LANDING-GEAR FLOW FIELD

Fei Li[1]
High Technology Corporation
Hampton, VA 23666

Mehdi R. Khorrami[2]
NASA Langley Research Center
Hampton, VA 23681

Mujeeb R. Malik[3]
High Technology Corporation
Hampton, VA23666

Abstract

This paper presents results of an unsteady Reynolds-averaged Navier-Stokes simulation of a landing-gear flow field. The geometry of the four-wheel landing-gear assembly consists of several of the fine details including the oleo-strut, two diagonal struts, a door, yokes/pin and a flat-plate simulating the wing surface. The computational results, obtained by using 13.3 million grid points, are presented with an emphasis on the characteristics of the unsteadiness ensuing from different parts of the landing-gear assembly, including vortex shedding patterns and frequencies of dominant oscillations. The results show that the presence of the diagonal struts and the door significantly influence the flow field. Owing to the induced asymmetry, vortices are shed only from one of the rear wheels and not the other. Present computations also capture streamwise vortices originating from the upstream corners of the door.

Introduction

During the approach and landing phase of an aircraft, the wing leading-edge slats and trailing edge flaps are fully extended and the landing gears are deployed. The interaction of the airflow with such protrusions in the aircraft structures gives rise to unsteady flow phenomena that are responsible for sound radiation. Because the engines are operated at reduced thrust during landing, airframe noise, especially from the landing gear and the high-lift system, constitutes a major noise source. The envisioned stricter community noise regulations are forcing aircraft manufacturers to devise ways to minimize noise radiation from the current and future large transport aircraft. Efficient noise prediction tools that incorporate the attendant physics are, therefore, highly desired and needed.

One approach towards this end is to numerically simulate the full complex flow field to provide the unsteady near-field pressure signature required by an acoustic solver based on the Ffowcs Williams-Hawkings formulation (Refs. 1 and 2), which then yields the acoustic far-field. Although computationally intensive, direct computation of the unsteady flow field provides an insight into the dominant noise sources which, in turn, can be used for developing reduced order models and in devising means for noise suppression. The combination of an accurate near-field flow solution with that of an acoustic propagation formulation has achieved considerable success in identifying noise sources associated with high-lift systems (e.g., Khorrami et al.,[3-5] Singer et al.[2,6]). The present study follows a similar approach and thus, as a first step towards a comprehensive goal of predicting landing-gear noise, highly resolved time-accurate flow simulation of a complex landing-gear configuration is attempted.

While flow computations of high-lift devices such as flaps and slats received significant attention in the last decade, the intricacies of a landing-gear flow field have remained essentially unknown due to overwhelming geometrical complexities. The multiple structures that collectively generate gear-related noise are nose landing gear, main landing gear (MLG), and wheel wells. Between the nose landing gear and the MLG, noise associated with the latter is louder and it is usually radiated in all directions. The wheel-well cavities produce high-amplitude tones. However, these tones occur at very low frequencies and hence are not considered important sources from the standpoint of community noise. In addition, experiments (Dobrzynski & Heller[7]) indicate that the landing gear protruding from the cavity provides a spoiling effect for the cavity tones. In view of these observations, the MLG noise constitutes the dominant part of the landing-gear noise.

[1] Senior Scientist, Member AIAA.
[2] Research Scientist, Computational Modeling and Simulation Branch, Associate Fellow AIAA.
[3] Chief Scientist, Associate Fellow AIAA.

Our current understanding of the landing gear generated noise comes from experiments performed mainly in Europe (e.g., Davy & Remy,[8] Dobrzynski et al.,[9] and Grosche et al.[10]), at least among those available in open literature. These experiments have indicated that, while the noise from high-lift devices is likely to dominate for mid-size aircraft, landing gear noise becomes more significant for large aircraft. It has also been found that the noise spectra associated with the landing gear are rather broad, ranging from a few hundred Hz to several kHz. Among the research work carried out in the U.S., Stoker et al.[11] has shown that the presence of the landing gear even impacts the noise associated with the flap system.

The present work is aimed at understanding the flow field associated with a representative MLG configuration. We perform Unsteady Reynolds-Averaged Navier-Stokes (URANS) computations for a relatively complex four-wheel landing gear assembly, including several of the fine details (e.g., yokes, pins, door, etc.). The model gear, designed to represent a Boeing 757 MLG, was tested (acoustically) in the Low Turbulence Pressure Tunnel (LTPT) at NASA Langley Research Center using a microphone array technique. The near-field preliminary computational results will be presented in this paper. The time-accurate flow field simulations will later be used for computation of landing gear associated far-field noise.

The first among the previous computational studies of landing gear flow field is the work reported by Strelets,[12] in which Detached Eddy Simulation (DES) technique was employed. Using this approach, incompressible Navier-Stokes equations were solved to simulate a relatively less detailed, symmetric, four-wheel landing gear configuration modeled by a total of 2.5 million grid points at a Reynolds number of 10^5.

More recently Souliez et al.[13] used an unstructured compressible Navier-Stokes solver for the same MLG configuration adapted here but without the door attached to the oleo and the flat-plate representing the wing surface. No RANS or Large Eddy Simulation (LES) model was used in their study, which employed a grid consisting of 1.2 million tetrahedral cells. With the aid of a Ffowcs Williams-Hawkings solver, the computed unsteady flow field was used to predict the noise field associated with the selected landing gear configuration.

In the present unsteady RANS simulation, we employ the thin-layer Navier-Stokes code, CFL3D,[14] where a multi-block structured grid consisting of 13.3 million grid points is utilized. The details of the computed flow field are presented in this paper. Computed wheel surface pressure variation is compared with experiments[15] performed on a similar, albeit much simpler, configuration. From the computational results, vortex shedding from the various components of the landing gear assembly is elucidated and the frequencies associated with dominant unsteady structures are given. The results also highlight the profound impact that diagonal struts and the door attached to oleo has on the flow field.

Landing-Gear Configuration and Computational Grid

The MLG geometry simulated in the present study is shown in Figure 1, where Cartesian coordinate system x, y, z is also shown. It consists of 4 wheels, 2 diagonal struts, an oleo-strut (the vertical pole), a side-door attached to the oleo, yokes/pin and other structures that join the system together. A flat plate (not shown in the figure) is attached to the top-end of the oleo and struts, which is meant to represent the aircraft wing. For the sake of computational efficiency however, the flat-plate boundary-layer is not finely resolved in the present study. Following the tested configuration in LTPT, a wheel-well cavity is also not simulated.

The wheel diameter is used as a reference length to non-dimensionalize the coordinate system. Note that in Fig. 1, x is in the free-stream direction and y is in the direction of the wheel axles with the $y = 0$ plane cutting through the center of the oleo. The vertical coordinate is represented by z with $z = 0$ plane cutting through the wheel centers. The top-most and bottom-most points of the wheels are situated at $z = 0.5$ and $z = -0.5$, respectively. The top flat-plate is at $z = 1.78237$. The computational boundary in the streamwise direction extends from $x = -5$ to $x = 13$ with $x = 0$ situated midway between the front and rear wheels. The streamwise gap between the two sets of wheels is 0.106 (i.e., 0.106 times the wheel diameter).

The constructed grid consists of 155 blocks with a total of 13.3 million grid points. To minimize overall number of grid points, moderate patching in certain blocks is invoked. On the solid surfaces (excluding the top wall), there are 247606 grid cells. Numerical tests were performed to assure that all the solid surface boundaries of the MLG and the grid-block interfaces are specified correctly. The grid distribution on the surface of the landing-gear is shown in Fig. 1 where every other grid point is displayed. Special attention was paid to appropriately model all the fine details of the MLG assembly.

In order to facilitate the subsequent presentations and discussions, we will refer to the four wheels of the landing gear system as front-left, rear-left, front-right and rear-right wheels, respectively, in the coordinate

system of an observer traveling with the landing gear and facing the incoming flow.

Computational Results

The flow solver used is CFL3D, developed at NASA Langley Research Center (Thomas et al.[16]). The two-equation k-ω turbulence model of Menter[17] is employed in this study. The parallel version of the code is used for the present computations, which are performed on the SGI-cluster at the National Aerodynamic Simulation (NAS) facility utilizing a total of 55 processors. To match the conditions of the NASA Langley LTPT experiment referred to above, present computations are conducted at a free-stream Mach number of 0.2 and a Reynolds number based on the wheel-diameter of 1.23×10^6. The free-stream static temperature is $302.9°K$ and the wheel diameter is $.094m$.

We first carried out steady-state computations on a coarser grid (i.e., half the resolution in each direction resulting in about 1.7 million total grid points) for 14,000 iterations using a CFL number of 0.5. This helped reduce the residual by at least two orders of magnitude. Subsequently, the time-accurate computations were started with a non-dimensional time-step of 0.01 ($\Delta t = \Delta t^* c_0 / d$, where d is the wheel diameter, c_0 is the speed of sound, and t^* is the time in seconds) on the same grid. With this time step, a particle in the free stream would travel a distance of one landing gear wheel-diameter in 500 time steps. We monitored the convergence of the inner iterations as well as data from computational probes in the flow field to ensure that a stable numerical solution was obtained. Once this was assured, the computation was switched (at t = 44.6) to the fine grid (13.3 million grid points) with a time step of 0.005. Calculations were then carried out up to a nondimensional time of 84.3.

MLG Surface Pressure

The unsteady pressure field on the landing gear surface (or on an imaginary surface around the landing gear assembly) is an input for the acoustic solver. Therefore, we first present computed surface pressure.

Figure 2 shows a perspective plot of instantaneous (at t = 84.3) pressure contours over the landing-gear surface viewed at an angle. The flow is from right to left. We notice that the red contours (high pressure) in the front of the two front wheels representing the neighborhood of the stagnation points do not lie on the respective centerlines of the wheels, but are shifted toward each other. Red contours also appear in the front of the oleo and the front of the front strut. The contour patterns on the rear-right wheel are much more complex as it is in the wake of the front-right wheel. A low-pressure region appears near the downstream side of the wheel, indicating high velocity in that region.

Figures 3 through 6 show the pressure coefficients ($c_p = 2(p - p_\infty)/\rho_\infty U_\infty^2$) along the mid-wheel circumference for 13 selected instances over a duration of approximately 20 non-dimensional time units. During this time period, a particle moving with the free-stream speed travels a distance of 4 wheel diameters. Note that the azimuthal angle of each wheel is measured from its front-most point. We refer to the upper side (see Fig. 1) of a wheel as the wing-side and the lower-side as the ground-side. Therefore, 90-degrees on the wing-side refers to the top-most point of a wheel, and 90-degrees on the ground side refers to the bottom-most point. Here, an angle of 180-degrees refers to the rear-most point.

Due to asymmetry of the flow (caused by the struts and the door) the stagnation points on the two front-wheels do not lie at the front-most points. Therefore, the pressure coefficients there are slightly smaller than 1. The distributions of pressure coefficients on the four wheels are different from each other, exhibiting different degrees of unsteadiness. We, therefore, discuss these results separately.

In Figure 3, the pressure on the front-left wheel drops as expected for a circular-shaped body. Minimum pressure is reached at an azimuthal angle of approximately 90 and 85 degrees for the wing-side and the ground-side, respectively. The pressure rises until approximately 140 and 130 degrees, respectively, on the wing-side and the ground-side. Then, the pressure coefficients computed at different instances start to drop and begin to have slight differences. This is an indication that flow is separated from these locations. Since the differences in pressure among the data computed at the 13 instances are small, the separations appear to be relatively steady.

In Figure 4, the same can be said about the pressure distribution on the wing-side of the front-right wheel, where little difference can be noticed among the 13 instances. However, the pressure on the ground-side is quite another story. The pressure coefficients for the 13 instances begin to show a significant difference around 70 or 80 degrees. For any fixed angle between approximately 70 and 100 degrees, the pressure decreases monotonically in time. (*i.e.* the pressure coefficient curve at an earlier instance appears above that at a later instance). This either indicates that the computed flow in the region is gradually converging to some steady state or that it is oscillating with a very low frequency. Further computations are required to

determine what exactly is happening in this region. Beyond 110 degrees the monotonic nature is lost, indicating that the flow is undergoing unsteady oscillations.

The different flow behavior around the two front wheels is a consequence of the asymmetric layout of the landing-gear system (*i.e.* the presence of the struts and the door), as noted above.

Figure 5 shows the pressure coefficients of the rear-left wheel. Since it is in the wake of the front-left wheel, its front-most point is nowhere near a stagnation point. Unsteadiness sets in at approximately 130 and 110 degrees, respectively, for the wing side and the ground side.

Figure 6 shows the pressure coefficients of the rear-right wheel. The ground side has large oscillations in pressure between approximately 10 and 90 degree locations. This is most likely caused by the impingement of the unsteady wake from the front-right wheel onto the rear-right wheel. Both the wing side and the ground side begin to experience significant unsteadiness from approximately 130 degrees on.

Lazos[15] carried out an experiment with a much simpler landing-gear assembly that consists only of an oleo and four wheels joined together by two axles and a cylindrical rod. In this case, the flow is symmetric with respect to the $y = 0$ plane. Furthermore, the sides of the wheels are flat and do not have the fine details of the wheels used in the present computation. Reynolds number in the experiment is 6×10^5 as compared to the present value of 1.23×10^6. Figure 7 shows the experimental results together with the present computational data. The measured pressure distribution around the front wheel shows the same general behavior as those of the present computation. However, it is seen that the pressure coefficient continues to decrease up to larger azimuthal angles for the experimental results as compared to the computations. We stress here that this comparison is not intended for quantitative validation of computational results, since the landing-gear assembly used in the computations and the experiment are not the same.

Probe Data

In order to investigate unsteadiness in the flow, we positioned a total of 4 probes at distinct locations to record the density, velocities and pressure. One probe is placed behind the axle of the rear-left wheel, a second probe is placed between the struts, a third probe is placed behind the mid-portion of the oleo and the last one is placed behind the lower portion of the oleo. Figure 8 shows the variation of pressure with time t (which is scaled with wheel diameter and speed of sound) at the fine grid level over a nondimensional time span of approximately 40. During this time span, a particle traveling with the freestream speed covers a distance of 8 wheel diameters.

We can observe that the initial high-frequency transients rapidly decay as time progresses. Yet, as the end of the time-record is approached, it is not obvious that the computed flow field has reached a quasi-steady state. Thus, it appears that the present unsteady flow field is still not suitable for providing the near-field pressure signature required by an acoustic solver. However, some interesting features of the flow are beginning to take shape.

The two probes behind the oleo begin to show some very high frequency, growing oscillations shortly after the fine-grid computation starts. While the high-frequency pressure oscillations recorded by the probe behind the lower oleo grow slowly, the probe behind the mid-oleo detects oscillations that grow relatively rapidly. Figure 9 shows the pressure fluctuations after the data from the probe behind the mid-oleo is processed by a high-pass filter. The initial growth appears to be exponential. Eventually, the pressure oscillations saturate at approximately 0.03% of the freestream pressure. The saturated amplitude of the corresponding velocity fluctuations (not shown) is approximately 0.15% of the freestream speed or approximately 3% of the local flow speed. A shorter time record of the pressure oscillations is shown in Figure 10, from which the oscillation frequency is determined to be approximately 24 kHz. Note that each period of oscillation in Fig. 10 is resolved by about 30 time steps.

Given the small amplitude of the oscillations, the probability that these oscillations originate from the vortex shedding off the oleo is small. In fact, preliminary analysis of the flow field data indicates that the source of the oscillations is, perhaps, the flow resonance in the gap between the door and the oleo. The eventual saturation of the oscillation amplitudes is likely due to two reasons: (1) as time progresses, the flow field reaches such a state that these oscillations become neutrally stable and (2) the amplitude of the oscillations becomes large enough for nonlinearity to play a part in bringing the exponential growth to a halt. The latter is plausible because of the high oscillation frequency and the relatively large amplitude with respect to local flow speed.

Flow Field

Now we discuss some of the notable features of the landing gear flow field, which include vortex shedding from various parts of the landing-gear system and

asymmetry of the passing flow as well as its consequences. Ideally, the unsteady flow field can be analyzed by saving computational data at intervals of a few time-steps for some extended duration so that the flow history at every point in the flow field can be obtained if necessary. This, of course, requires an enormous amount of hard-disk space since the file containing density, velocity components and internal energy of the flow field for one instance in time is approximately 253 MB in size. Assuming that the computational data on every other time-step for a nondimensional time period of 20 (*i.e.*, time taken by a particle traveling with the freestream speed to cover a distance of 4 wheel-diameters) is required, then, with a time step of 0.005, the disk space needed will be 506 GB. Since currently the flow field has not reached a quasi-steady state, we choose not to take this path at this time. Instead, we save the computational data at 13 discrete instances (not quite evenly spaced) starting from $t = 73.6$ and ending at $t = 84.3$.

We first consider the flow in the horizontal plane $z = 0$ that cuts through the centers of all four wheels. Figures 11 and 12 show, respectively, the instantaneous density and spanwise velocity contours at $t = 84.3$. Vortices are being shed from the rear-right wheel but not from the rear-left wheel. This must be due to the fact that the flow is asymmetric with respect to the centerline dividing the two rows of wheels. At all other 12 instances the shedding patterns are similar. The shedding frequency is estimated to be approximately 800 Hz.

We note that the shedding pattern is different from that of a typical blunt body in that, instead of two rows of vortices coming off the wheel alternately from either side, only one row of vortices is seen. The density contours in Fig. 11 resemble those of a plane shear layer. The shear-layer instability mechanism is likely responsible for this shedding pattern. The speed of flow past rear-right wheel on the right hand side is higher than that on the left hand side because of the blockage effects of the solid blocks, the oleo and the wheel-axles, creating a strong enough local shear layer so that Kelvin-Holmholtz type of instability sets in. As the horizontal plane is moved up or down (*i.e.* out of or into the paper), the shedding pattern seems to diminish and eventually disappear. The flow in the plane is highly three-dimensional with the vertical (z) velocity amplitude being of the same order as that of the spanwise (y) velocity.

We now investigate vortex shedding behind the struts. A horizontal plane at $z = 1.3$ is chosen so that it cuts through the mid-portion of the struts. Note that $z = 0.5$ signifies the top-most points of the wheels. Figures 13 and 14 show the density and spanwise velocity contours in this plane at $t = 84.3$. The vortex shedding appear to be alternating from either side of the downstream strut. The shedding frequency is estimated to be approximately 600 Hz. No vortices seem to be shed from the oleo/door assembly.

As mentioned earlier, the flow past the landing gear system is asymmetric with respect to the plane $y = 0$ (*i.e.* the plane bisecting the wheel axles). Therefore, the flow patterns on the left and on the right are different. This asymmetry is already apparent at some distance upstream of the landing gear. Figure 15 shows contours of streamwise velocity at a distance of approximately half a wheel diameter upstream of the front ends of the wheels. The presence of the components of the landing gear system is already sensed by the flow.

Figure 16 shows the contours of streamwise velocity in the x-plane close to the rear of the rear wheels. Regions of reverse flow exist behind the door/oleo and the struts, and between the wheels. There is also a high velocity region on the right side of the rear-right wheel. This high velocity region is possibly responsible for the shear-layer type of vortex shedding discussed earlier. The presence of the struts forces the flow to go around the struts and causes the flow over the rear-right wheel to be faster than that over the rear-left wheel.

Figure 17 shows the contours of streamwise velocity at a distance of approximately half a wheel-diameter downstream of the back ends of the wheels. The features seen in Fig. 16 are further amplified here. However, there is no backflow at this x location. In both Figs. 16-17, a vortex can be seen near the oleo/flat-plate junction. The origin of this vortex will be discussed later.

Figure 18 shows the streamwise velocity contours in the $y = -0.463$ plane that cuts through the left wheels. The wake behind the left wheels does not appear to have an identifiable wave structure. Near the top wall is a slow-flow region that starts just after the x-location of the oleo. This is, in fact, inside the vortex earlier seen in Figs. 16-17.

Figure 19 shows the results in the plane ($y = 0.463$) containing the right wheels. The wake behind the right wheels exhibits strong waviness, consistent with what is discussed earlier (Fig. 11). This plane also cuts through the two struts (note the two thin, rectangular slits above the wheels). The wake from the struts tends to accelerate the flow around the rear-right wheel. This is made more clear in Fig. 20, which gives a close-up view of the velocity contours shown in Fig. 19. The reverse flow regions behind the wheels and the struts, and the fast flow region between the strut-wake and the rear-right wheel are clearly seen. Note that the range of

velocity contours (-0.1 to 0.25) in Fig. 20 was selected to show the overall details of the flow field in the selected plane. However, the maximum (0.311) and minimum (-0.1605) streamwise velocities occur outside this range. The maximum velocity occurs in the small hollow region on top of the rear wheel, while the minimum velocity occurs in the hollow region near the lower right part of the front wheel.

An interesting feature of the flow is that the flow coming towards the door is incident at an angle to the plane containing the door and, therefore, the flow separates at the leading edge of the door and never reattaches to it. Figure 21 shows the streamwise velocity contours at the plane $z = 1.3$ in the vicinity of the door. Reverse flow is clearly seen. Figure 22 shows streamwise velocity profiles in the vertical plane $x = 0.15$ cutting through the door slightly ahead of the rear wheels. A vortex on the door-top can be clearly seen. The origin of this vortex is the upstream top-corner of the door. The signatures of this streamwise vortex were earlier seen in Figs. 16-18. We note that another vortex is present near the lower part of the door which originates from the upstream lower-corner of the door. While this vortex seems to merge with the rest of the flow field, its signature can be seen in Fig. 16 near the top of the left wheel. In between the top and bottom tip-vortices, there exists a region of reverse flow.

The small spaces between the yoke and the door also produce high-frequency oscillations. Figure 23 shows pressure contours on the surface of the door downstream of the oleo. Islands in the vicinity of junctions of door, yoke, etc. are signatures of the high frequency waves. Several probes will need to be placed in these locations to determine the frequencies accurately. In order to provide the unsteady pressure field for his acoustic solver, Lockard[18] continued our coarse grid (1.7 million nodes) simulation for a much longer time period. In that case, a probe behind the lower portion of the oleo picked up high frequency oscillations (see Figure 24) including a frequency of 25.4 kHz, which is close to the value of 24 kHz referred to above.

Conclusions

RANS simulations of unsteady flow past a landing-gear assembly, which consists of four wheels, axles, connecting blocks, a door, an oleo and two struts, are carried out. The oleo and the diagonal struts are attached to a flat-plate to simulate the wing surface. The grid consists of 155 block with a total of 13.3 million grid point. Computations are performed on the SGI-cluster at the NAS facility utilizing a total of 55 processors. The flow has a Mach number of 0.2 and a Reynolds number of 1.23×10^6.

Computational results show that vortex shedding with a frequency of approximately 800 Hz occurs off the rear-right wheel, i.e., the one on the side of the diagonal struts. Vortex shedding at a frequency of about 600 Hz also occurs off the downstream strut. Pressure fluctuations with a frequency of about 24 kHz are found behind the mid-portion of the oleo. The results also indicate that the flow separates at the leading edge of the door and never reattaches. While the flow around the rear-right wheel undergoes strong oscillations, there is no evidence of such oscillations from the left wheel. This flow asymmetry is caused by the geometric asymmetry induced by the presence of the diagonal struts and the door attached to the oleo. Computations also show the existence of streamwise vortices that originate from the top and bottom upstream corners of the door.

Acknowledgements

This research work was made possible by the financial support provided to High Technology Corporation under NASA Contract NAS1-00088 through a Lockheed Martin subcontract.

References

1. Ffowcs Williams, J. E. and Hawkings, D. L., "Sound Generation by Turbulence and Surfaces in Arbitrary Motion," *Philosophical Transactions of the Royal Society of London A*, Vol. 342, 1969, pp. 264-321.

2. Singer, B. A., Brentner, K. S., Lockard, D. P., and Lilley, G. M., "Simulation of Acoustic Scattering from a Trailing Edge," *J. of Sound and Vibration*, Vol. 230, No.3, 2000, pp. 541-560.

3. Khorrami, M. R., Berkman, M., and Choudhari, M., "Unsteady Flow Computations of a Slat with a Blunt Trailing Edge," *AIAA J.*, Vol. 38, No.11, November 2000, pp. 2050-2058.

4. Khorrami, M. R., Singer, B. A., and Berkman, M. E., "Time-Accurate Simulations and Acoustic Analysis of Slat Free Shear Layer," AIAA Paper 2001-2155, 2001.

5. Khorrami, M. R., Singer, B. A., and Radeztsky, Jr., R. H., "Reynolds Averaged Navier-Stokes Computations on a Flap Side-Edge Flow Field," AIAA Paper 98-0768, 1998.

6. Singer, B. A., Lockard, D. P., and Brentner, K. S., "Computational Aeroacoustic Analysis of Slat Trailing-Edge Flow," *AIAA J.*, Vol. 38, No.9, September 2000, pp. 1556-1564.

7. Heller, H. H. and Dobrzynski, W. M., "Sound Radiation from Aircraft Wheel-Well/Landing-Gear Configurations," *J. Aircraft*, Vol. 14, No. 8, 1977, pp. 768-774.

8. Davy, R. and Remy, H., "Airframe Noise Characteristics of a 1/11 Scale Airbus Model," AIAA Paper 98-2335, 1998.

9. Dobrzynski, W. M. and Buchholz, H., "Full-Scale Noise Testing on Airbus Landing Gears in the German Dutch Wind Tunnel," AIAA Paper 97-1597-CP, 1997.

10. Grosche, F.-R., Schneider, G., and Stiewitt, H., "Wind Tunnel Experiments on Airframe Noise Sources of Transport Aircraft," AIAA Paper 97-1642, 1997.

11. Stoker, R. W. and Sen, R., "An Experimental Investigation of Airframe Noise Using a Model-Scale Boeing 777," AIAA Paper 2001-0987, 2001.

12. Strelets, M., "Detached Eddy Simulation of Massively Separated Flows," AIAA Paper 2001-0879, 2001.

13. Souliez, F. J., Long L. N., Morris P. J. and Sharma A., "Landing Gear Aerodynamic Noise Prediction Using Unstructured Grids," AIAA Paper 2002-0799, 2002.

14. Krist, S. L., Biedron, R. T. and Rumsey, C. L., "CFL3D User's Manual," NASA TM-1998-208444, 1998.

15. Lazos, B. S., "Mean Flow Features Around the Inline Wheels of Four-Wheel Landing Gear," *AIAA J.*, Vol. 40, No. 2, 2002, pp. 193-198.

16. Thomas, J., Krist, S., and Anderson, W., "Navier-Stokes Computations of Vortical Flows Over Low Aspect-Ratio Wings," *AIAA J.*, Vol. 28, 1990, pp. 205.

17. Menter, F. R., "Zonal two-equation k-omega turbulence Models for Aerodynamic Flows," AIAA Paper 1993-2906, 1993.

18. Lockard, D., "A Comparison of Ffowcs Williams-Hawkings Solvers for Airframe Noise Applications," AIAA Paper 2002-2580, 2002.

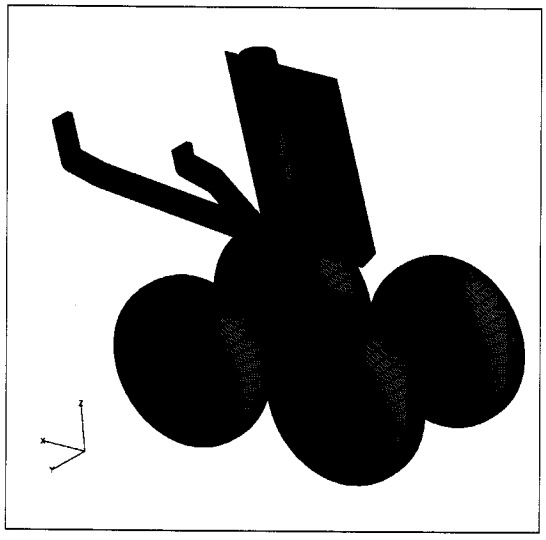

Figure 1. Grid distribution over landing gear surface. Every other grid point is shown. The oleo and the two diagonal struts attach to a flat-plate (not shown).

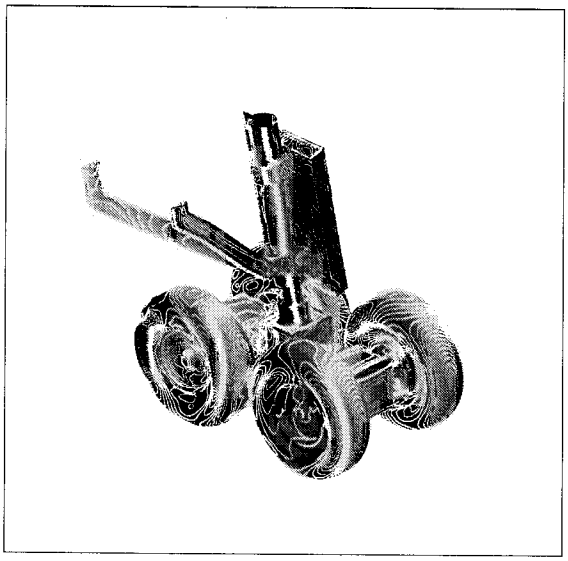

Figure 2. Perspective plot of instantaneous pressure contours. Flow from right to left.

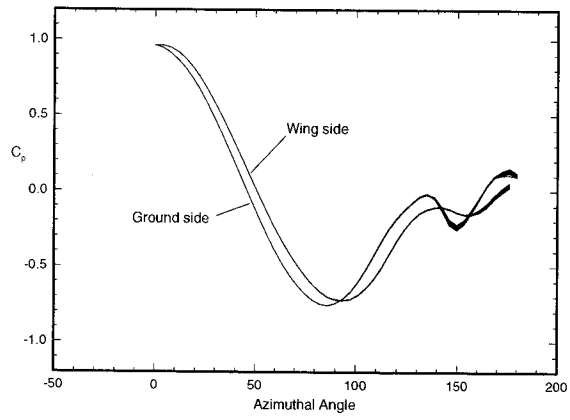

Figure 3. Variation of pressure coefficient around the (mid-wheel) circumference of the front-left wheel at 13 selected time instances.

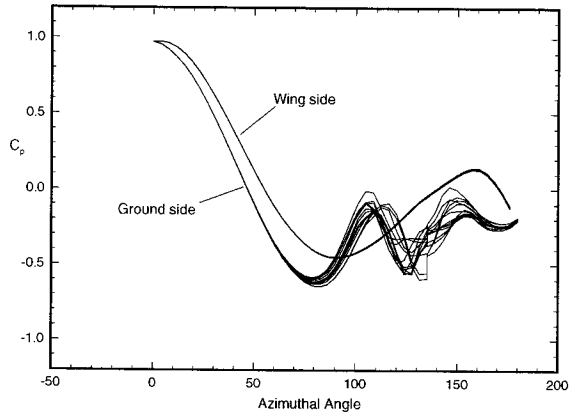

Figure 4. Same as in Fig. 3 except for the front-right wheel.

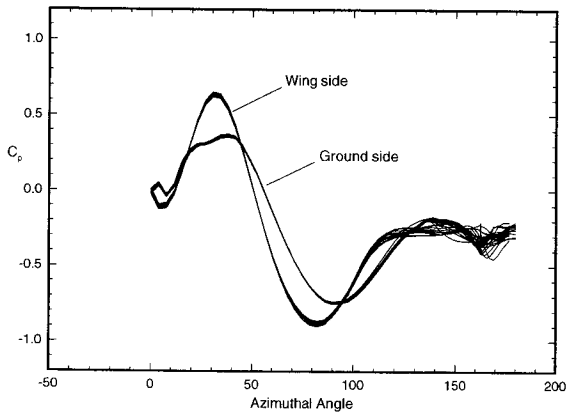

Figure 5. Same as in Fig. 3 except for the rear-left wheel.

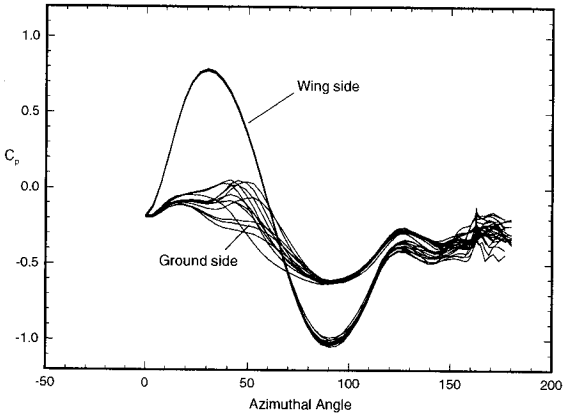

Figure 6. Same as in Fig. 3 except for the rear-right wheel.

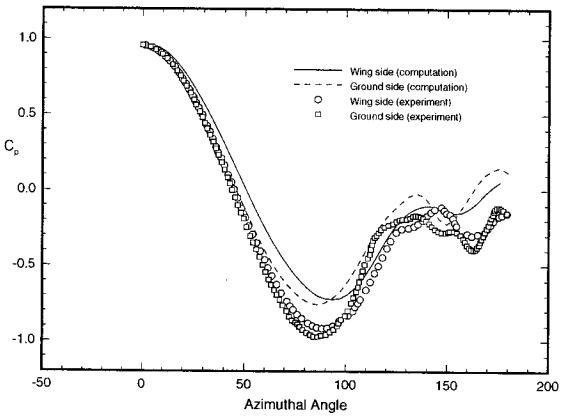

Figure 7. Pressure coefficient around the circumference of the front-left wheel. Comparison with experiment. MLG geometries used in the experiment and the computation are not the same.

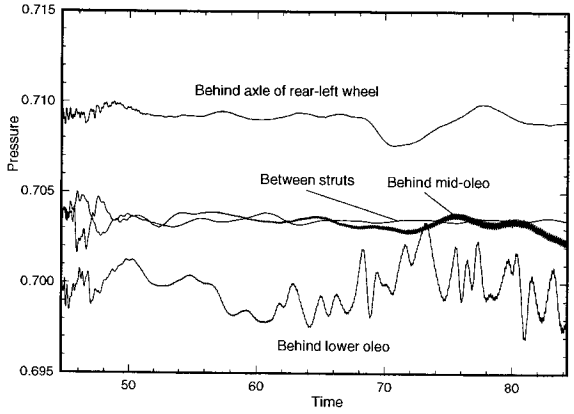

Figure 8. Pressure data from four probes.

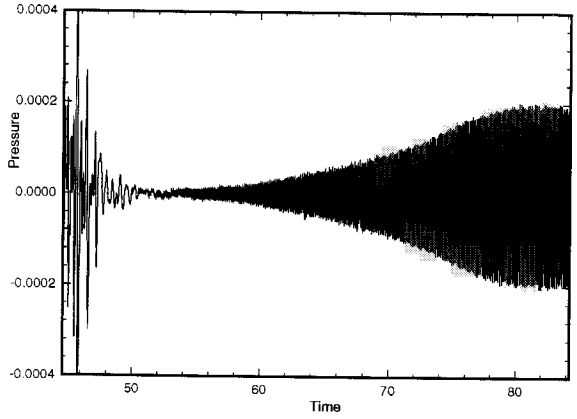

Figure 9. High-pass filtered pressure data from probe behind mid-oleo.

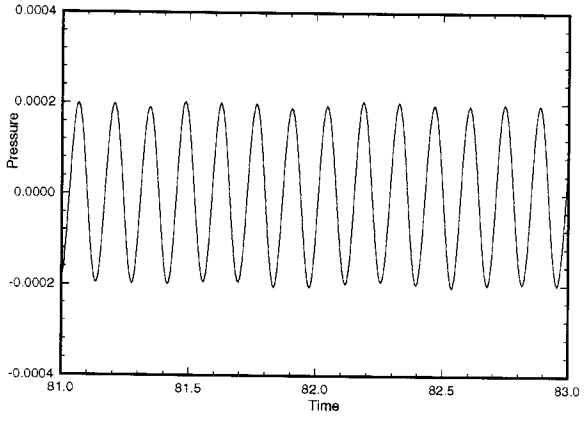

Figure 10. A shorter time record of high-pass filtered pressure data of Fig. 9. The frequency of oscillation is 24 KHz.

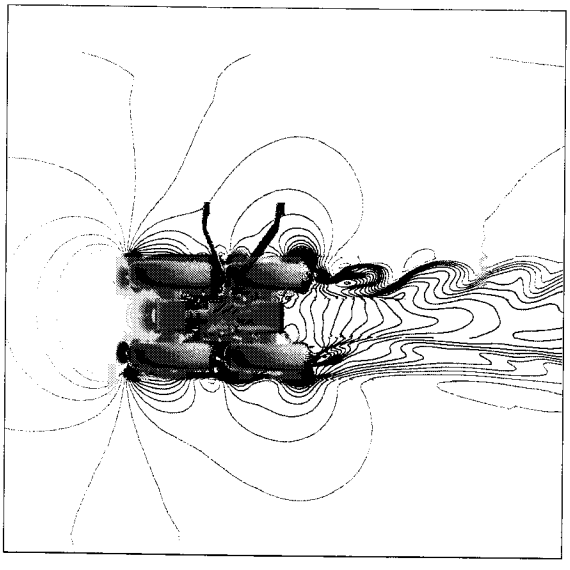

Figure 11. Density contours in the z = 0 plane at t = 84.3 (blue: 0.97 and red: 1.02).

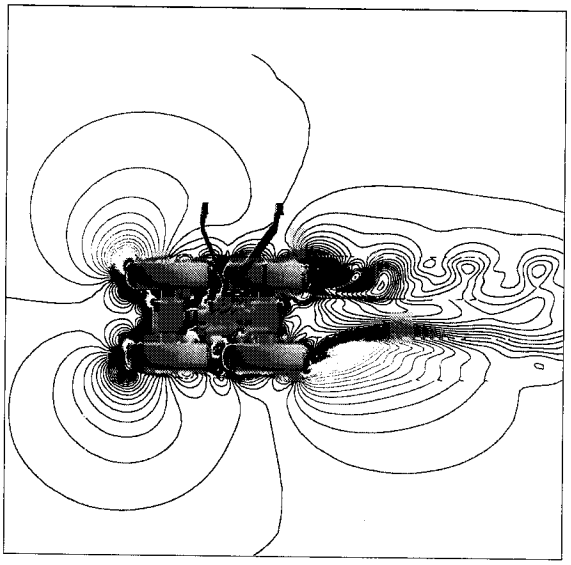

Figure 12. Spanwise velocity contours in the z = 0 plane at t = 84.3 (blue: -0.12 and red: 0.12).

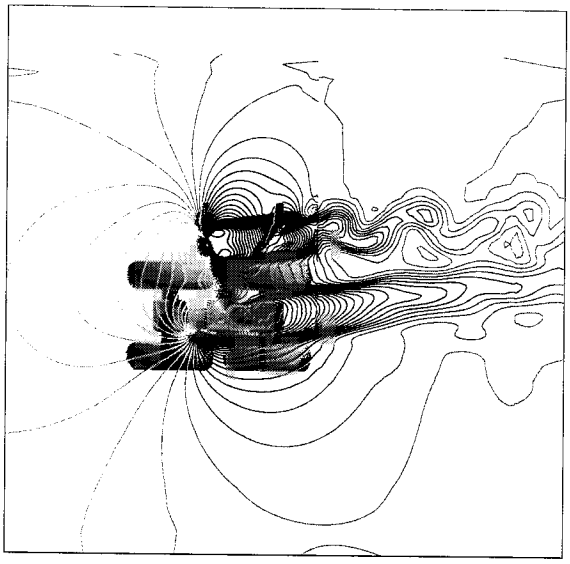

Figure 13. Density contours in the z = 1.3 plane at t = 84.3 (blue: 0.97 and red: 1.02).

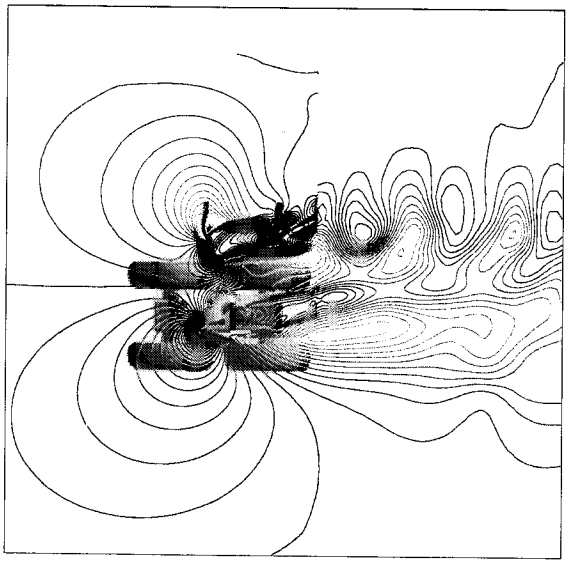

Figure 14. Spanwise velocity contours in the z = 1.3 plane at t = 84.3 (blue: -0.12 and red: 0.12).

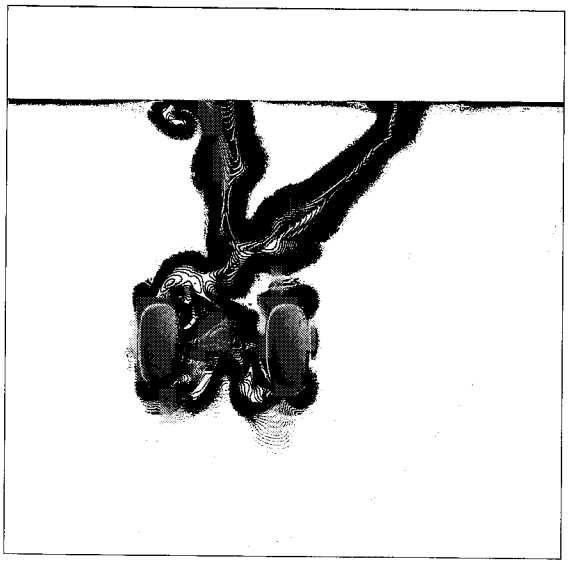

Figure 16. Streamwise velocity contours in the x = 0.95 plane at t = 84.3, as viewed from downstream (blue: -0.1 and red: 0.35).

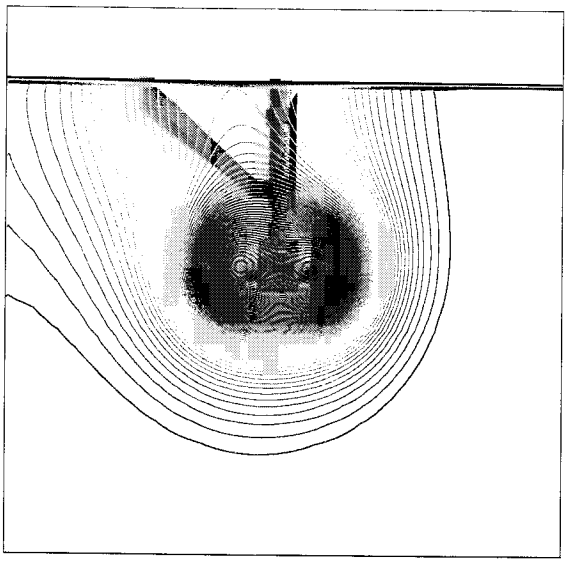

Figure 15. Streamwise velocity contours in the x = −1.5 plane at t = 84.3, viewed from upstream (blue: 0.17 and red: 0.2).

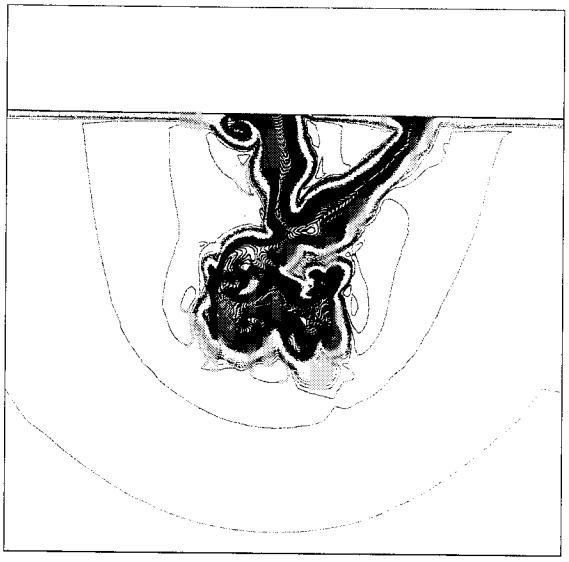

Figure 17. Streamwise velocity contours in the x = 1.5 plane at t = 84.3, as viewed from downstream (blue: 0.0 and red: 0.2).

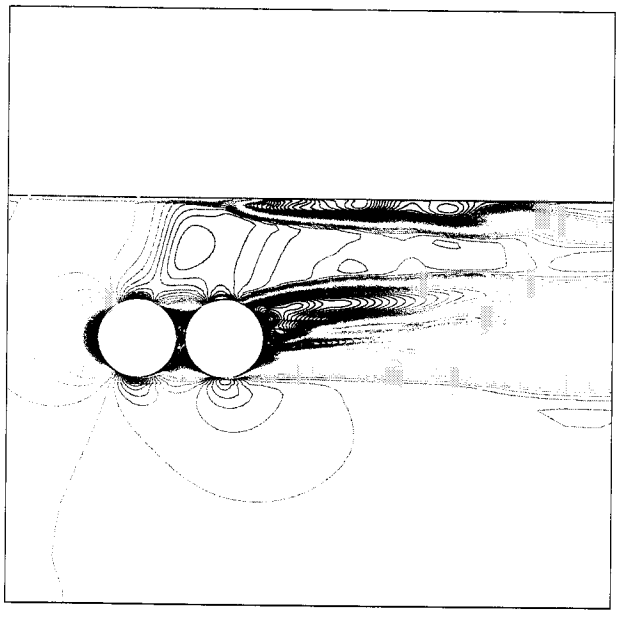

Figure 18. Streamwise velocity contours in a plane cutting through the left wheels at $y = -0.463$ (blue: –0.1 and red: 0.25).

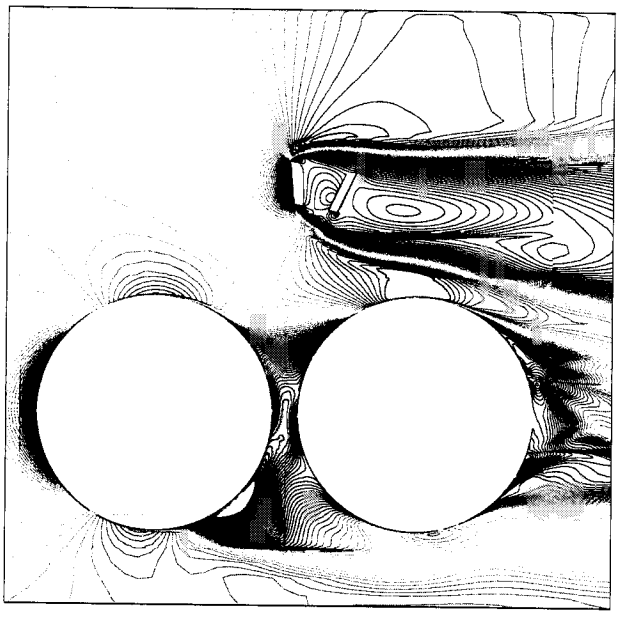

Figure 20. An enlarged view of results in Fig. 19.

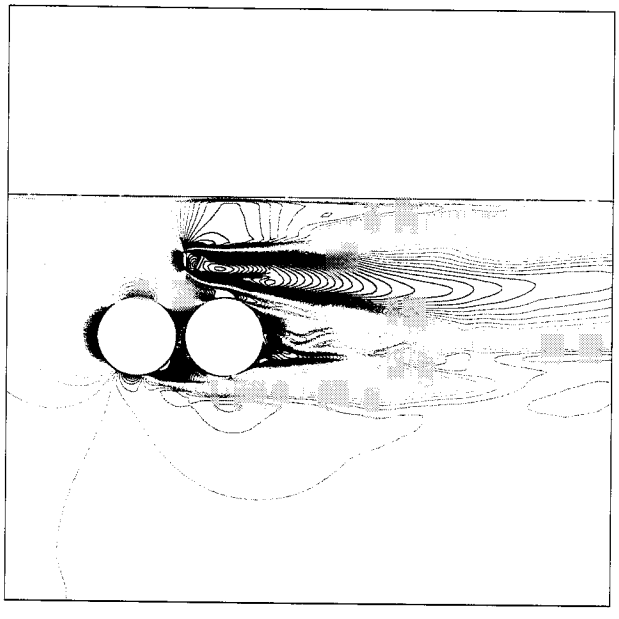

Figure 19. Streamwise velocity contours in a plane cutting through the right wheels at $y = 0.463$ (blue: -0.1 and red: 0.25).

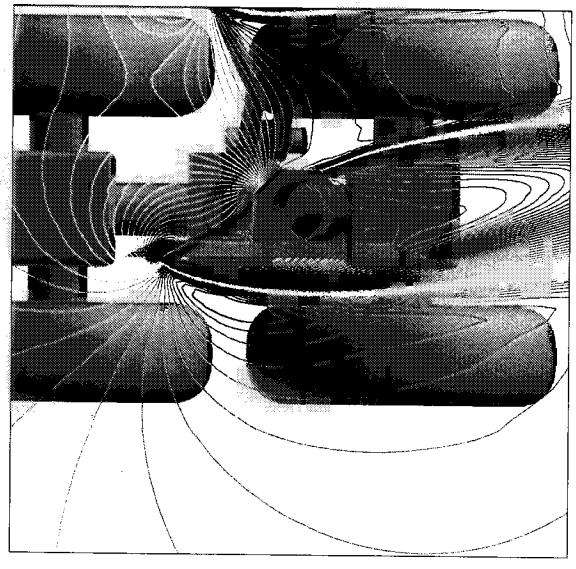

Figure 21. Streamwise velocity contours in the plane $z = 1.3$. Reverse flow is seen near the surface of the door indicating flow separation (blue: –0.1 and red: 0.25).

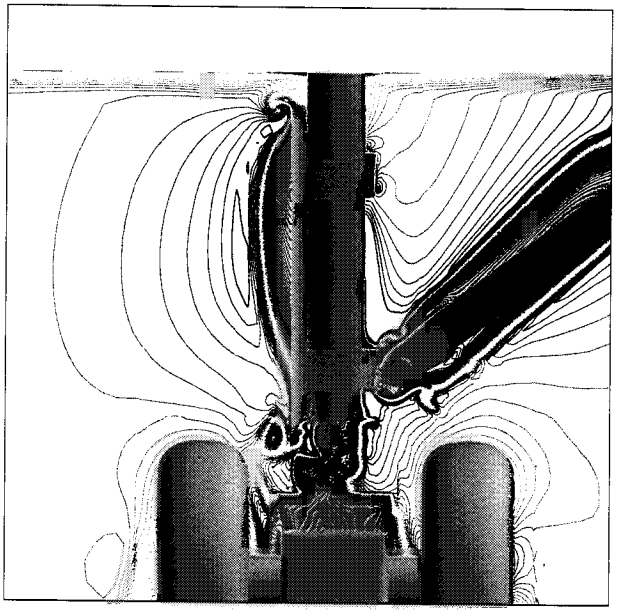

Figure 22. Streamwise velocity contours in x = 0.15 plane at t = 84.3, as viewed from downstream (blue: –0.1 and red: 0.25).

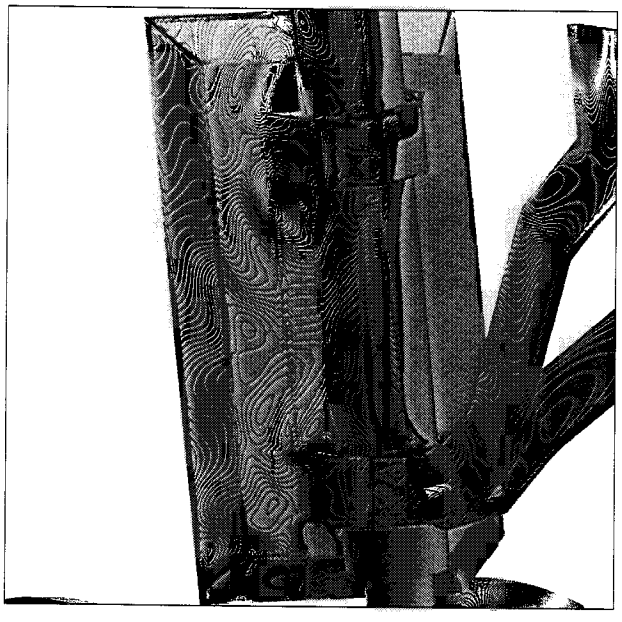

Figure 23. Pressure contours on the surface of the door. Islands in the vicinity of junctions of door, yoke and oleo are signatures of high-frequency waves (blue: 0.70 and red: 0.71).

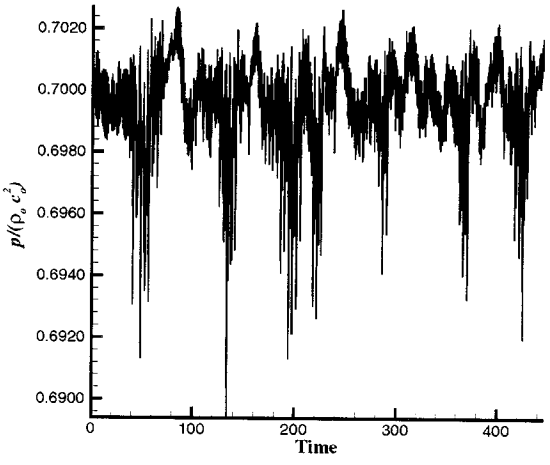

Figure 24. High frequency oscillations behind lower oleo. From Lockard.[18]